Contents lists available at ScienceDirect

International Journal of Applied Earth Observations and Geoinformation

Towards analysis ready data of optical CubeSat images: Demonstrating a hierarchical normalization framework at a wetland site

Zhan Li [a,b,*], Daniel Scheffler [a], Nicholas C. Coops [c], Nicholas Leach [c], Torsten Sachs [a]

[a] Remote Sensing and Geoinformatics, Helmholtz Centre Potsdam, GFZ German Research Centre for Geosciences, Telegrafenberg, 14473 Potsdam, Germany
[b] Department of Remote Sensing, Helmholtz Centre for Environmental Research – UFZ, Leipzig 04318, Germany
[c] Integrated Remote Sensing Studio, Faculty of Forestry, University of British Columbia, 2424 Main Mall, Vancouver, BC V6T1Z4, Canada

ARTICLE INFO

ABSTRACT

Optical images of the Earth at very high spatial resolutions (VHR, typically < 5 m) are seeing rapid growth in volumes over the past 5 years, due in part to the fast-expanding constellations of CubeSats. Special preprocessing of these VHR images is required to ensure their geometric and radiometric consistency for quantitative analyses for a wide range of Earth and environmental sciences and applications. Here we describe a hierarchical normalization framework (HiNF) to achieve and evaluate geometric and radiometric normalization of these VHR images towards producing analysis ready data (ARD) of optical CubeSat images. We demonstrated HiNF at a spatially heterogeneous and temporally dynamic wetland site in northeastern Germany by generating a stack of temporally consistent ~ biweekly 5-m images over 8 years (2013–2020) at visible and near infrared bands (VNIR). The HiNF combined images from rigorously calibrated multispectral sensors onboard large satellites (Landsat-7/8 and Sentinel-2) and less well calibrated sensors onboard RapidEye (SmallSats) and PlanetScope (CubeSats). A two-stage radiometric normalization procedure produced two levels of image normalization and resulted in more normalized images that passed the quality control in time series compared to common one-stage procedures. The outcome of this novel procedure allows for downstream applications to balance between the quality and the quantity of available normalized CubeSat images in a time series. The HiNF provides a new approach to quantitative evaluations of radiometric normalizations using daily MODIS imagery as bridging benchmark data. The quantitative evaluations showed the HiNF resulted in greater normalization efficacy in the visible bands than in the NIR over the predominantly wetland area. The two normalization levels yielded statistically similar efficacy for the NIR band and the widely-used normalized difference vegetation index according to the Chow test (at significance level of 0.05) but less so for the visible bands. The HiNF facilitates generating ARD of optical CubeSat images and assuring their qualities through its demonstrated efficacy and its quantitative evaluation approach. Such ARD-quality time series of VHR images from CubeSats allow for improved analyses and quantitative applications of this new stream of multispectral images at spatial scales that are better related to ground measurements and environmental management in terrestrial ecosystems.

1. Introduction

CubeSats are low-cost and miniaturized satellites made of commercial off-the-shelf components (Lee et al., 2020). The low costs and miniature sizes allow them to be launched in bulk into low Earth orbits (Puig-Suari et al., 2001), which facilitate the establishment of constellations comprising large numbers of satellites. Such constellations provide multipoint sensing of the earth and thus enhance observational coverages, enabling Earth observations (EO) at unprecedented spatial

and temporal resolutions that are impractical for traditional large satellites to achieve (Poghosyan and Golkar, 2017). A key example is the fast-expanding constellations of CubeSats carrying optical multispectral sensors, one of the most used sensor types in remote sensing of terrestrial ecosystems (Dash and Ogutu, 2016). For example, as one of the most recognized operators of CubeSat constellations, Planet (also known as Planet Labs, Inc.) currently provides optical images of the entire globe in the visible and near-infrared (VNIR) bands at a spatial resolution of ~3.7 m and a daily and even sub-daily revisit through its PlanetScope

constellation of 130 + CubeSats called "Doves" (Planet Labs Inc., 2021a).

Compared to large EO satellite missions at decameter resolutions such as Landsat and Sentinel-2, the higher spatial and temporal resolutions from CubeSat constellations offer extra spatiotemporal details about the land surface and better chances to relate satellite observations to ground data at relevant scales of field surveys and land management such as cropland farming and forest inventories. Some recent studies have demonstrated the opportunities to advance a wide range of earth and environmental sciences and applications via optical CubeSat images at very high resolutions (VHR, typically < 5 m) despite their limited spectral bands and spectral resolutions, such as in hydrology (Cooley et al., 2019; McCabe et al., 2017), ecology (Riihimäki et al., 2019), agriculture (Aragon et al., 2018; Cai et al., 2019), and disaster management (Santilli et al., 2018).

However, there are several concerns about the quality of optical CubeSat images for quantitative analyses in scientific investigations and monitoring applications (Dash and Ogutu, 2016; Houborg and McCabe, 2016; Selva and Krejci, 2012). First, operational onboard radiometric calibration of CubeSats is lacking or limited, making it difficult to ensure radiometric consistency through time, a prerequisite for long-term monitoring (Chander et al., 2010), both within and among sensors onboard many CubeSats. Second, large numbers of optical CubeSats in a constellation also imply possibly quite different atmospheric and illumination conditions in CubeSat images as a result of wide-ranging overpass time, and hence additional difficulties to spatially mosaic and/or temporally stack these CubeSat images for large-area time series analysis of EO images.

The requirements and benefits for large-area time series analysis of EO images have been well proven by recent applications of long-term Landsat imagery archive (Wulder et al., 2019) and the ongoing efforts towards analysis ready data (ARD) of Landsat (CEOS, 2021; Dwyer et al., 2018; Frantz, 2019). The generation of ARD data provides observations that are geometrically and radiometrically consistent and have non-target/poor-quality observations flagged. As such, ARD allow immediate large-scale analysis and interoperability through space and time with a minimum of additional user effort. Generating ARD from optical CubeSat images, however, faces greater challenges due to their aforementioned problems. Studies are emerging to push towards ARD of optical CubeSat images by leveraging existing or developing new algorithms of geometric co-registration and radiometric normalization of optical images (Houborg and McCabe, 2018; Kimm et al., 2020; Leach et al., 2019; Wang et al., 2020; Wegmueller et al., 2021; Wu et al., 2021). In general, these emerging studies generate temporally-consistent imagery stacks by normalizing CubeSat images to some reference images that are usually multispectral images from rigorously-calibrated sensors onboard large satellites.

To achieve ARD of optical CubeSat images, different normalization approaches, more sources of reference images, and additional processing steps need to be further tested and assessed. Here we present a hierarchical normalization framework (HiNF) that allows for flexible accommodations of different algorithms of geometric co-registration and radiometric normalization as well as for quantitative evaluation of normalization efficacy. The aim of the study is to layout major requirements on data, processing, and algorithms regarding the aforementioned needs towards ARD of optical CubeSat images through an example of demonstration. In the demonstration, we brought together some selected existing automatic algorithms for most processing needs. When a processing need is not yet well addressed by automatic algorithms, we used a manual approach for demonstration purpose and discuss the algorithm development needs. Below after describing the study area for the demonstration, we explain the requirements on data, processing, and algorithms in the HiNF by walking through the demonstration example. Then we present the results of the demonstration before discussing the potential and limitation of the HiNF and the future work to achieve ARD of optical CubeSat images.

2. Study area

Our study area is centered on the FLUXNET (FLUXNET Network, 2021) site Zarnekow (DE-Zrk) in northeastern Germany, an ecosystem-atmosphere heat and carbon flux monitoring site located within a rewetted minerotrophic peatland in the Peene River Valley (53°52.5′ N, 12°53.3′ E) (Fig. 1). The area has been subject to drainage for agricultural purposes since the 18th century, which was strongly intensified starting in the 1960s. In the winter of 2004/2005, the area was rewetted resulting in permanent inundation and the development of an open water surface surrounded by emergent vegetation dominated by *Typha latifolia*. Temporary drying of the shallow water body in the summer of 2016 triggered an expansion of the surrounding vegetation, which accelerated during and after a longer drought period in 2018. The highly dynamic vegetation development in recent years along with the dynamic hydrological conditions requires a temporally and spatially highly-resolved quantitative analysis in support of ongoing investigations of heat and carbon flux at the site (Franz et al., 2016; Koebsch et al., 2020).

3. Description of the HiNF

The goal of the HiNF is to generate stacks of temporally-consistent optical CubeSat images at or near the quality level of ARD. The design of the HiNF considers the following three issues, (1) flexibility of accommodating different algorithms for common processing steps in generating optical imagery ARD, namely, geometric registration, radiometric normalization, and cloud/cloud shadow detection; (2) applicability to different extents of region of interests; (3) objectivity in evaluating normalization efficacy. The first consideration on algorithmic flexibility is driven by the fact that the best algorithms may change for different applications. The second consideration on extent applicability recognizes the current reality that most CubeSat images are not open data, and the areal coverages of available CubeSat images vary from case to case. The third consideration on evaluation objectivity emphasizes quantifying normalization efficacy for downstream analyses and algorithm intercomparisons.

The HiNF (Fig. 2) has four stages of processing, each consisting of required processing steps. The Stage 1 & 2 ask for algorithms to adjust input CubeSat images for radiometric consistency while accounting for geometric misalignment. The Stage 3 asks for algorithms to flag non-target/poor-quality pixels, co-register CubeSat images and furnish the final stack of CubeSat images. The Stage 4 asks for algorithms to quantitatively evaluate normalization efficacy. We describe the required imagery data inputs by the HiNF in the Section 3.1, then Stage 1 & 2 in the Section 3.2 and Stage 3 & 4 in the Section 3.3. Although we focus on detailing the algorithms used in our demonstration example, other algorithms of similar types can be fit into the HiNF according to users' resources and needs.

3.1. Imagery data inputs in the HiNF

The HiNF (Fig. 2) combines three types of input images, (1) preliminary surface reflectance (SR) images at very high resolutions from CubeSats (referred as CubeSat images); (2) ARD-level SR images at decameter resolutions acquired by near-nadir observing and narrow-/medium-swath sensors onboard large satellite constellations, such as Landsat and Sentinel-2 (referred as Landsat-like images); (3) ARD-level daily SR images at hectometer resolutions acquired by wide-swath sensors onboard large satellite constellations, such as MODIS on Aqua/Terra and VIIRS on Suomi-NPP (referred as MODIS-like images). Although it is more likely to pair MODIS-like images of daily resolutions with CubeSat images on the same day, the wide disparity in the spatial resolutions of the two imagery sources are disadvantageous to geometric co-registration and radiometric normalizations. Alternatively, Landsat-like images are available at least every 16 days (acquisition by one
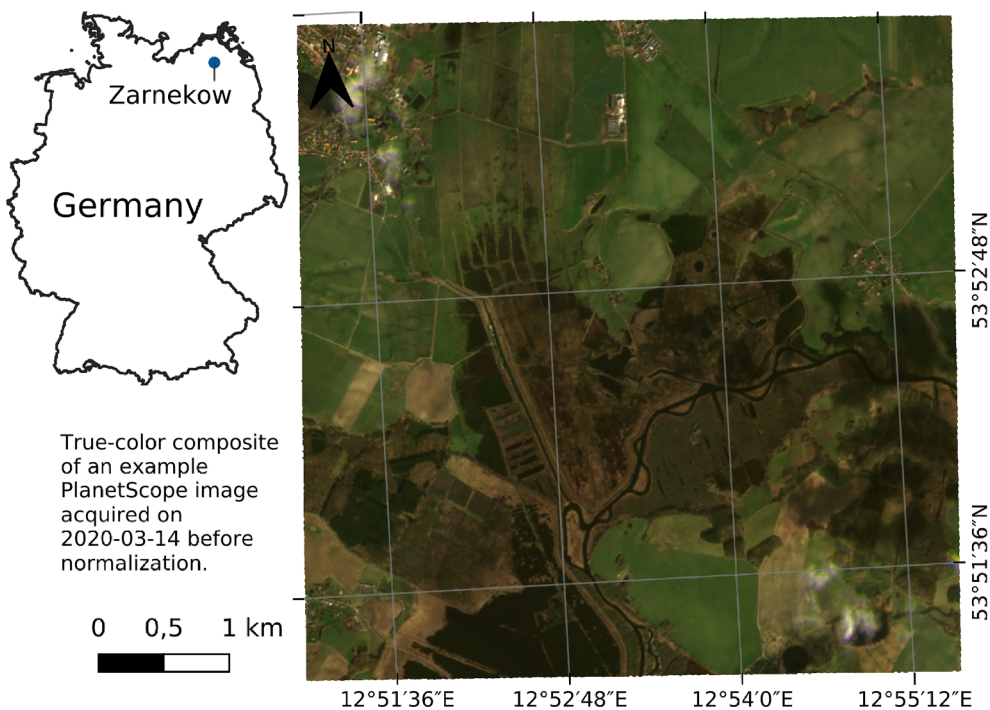
Fig. 1. Overview of the study area, Zarnekow, a wetland site in northeast Germany.
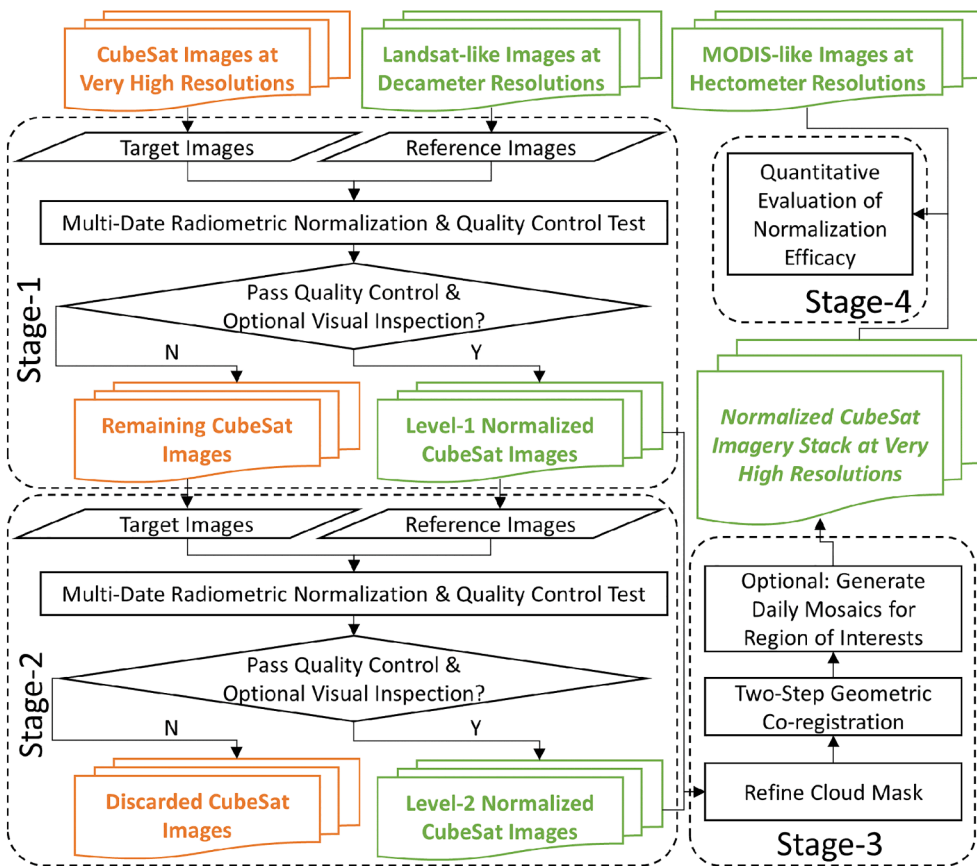

Fig. 2. A diagram to illustrate Hierarchical Normalization Framework (HiNF).

Landsat satellite) or as short as every 3 days (combined acquisition by Landsat-8 and two Sentinel-2 satellites). Potential changes between the acquisition dates in paired CubeSat and Landsat-like images can be dealt with by adapting some existing algorithms originally designed for multitemporal image normalization (Canty et al., 2004; Canty and Nielsen, 2008; Du et al., 2002; Zhang et al., 2014). Therefore, we choose

to rely on decameter Landsat-like SR images that are available every few days for the generation of temporally-consistent CubeSat images while relying on daily MODIS-like SR images at hectometer resolutions for quantitative evaluation of normalization efficacy.

In our demonstration example, we generated an 8-year temporal stack of normalized VHR images from two satellite constellations, RapidEye (year 2013 to 2016) and PlanetScope (year 2016–2020) (Planet Labs Inc., 2021a). Although RapidEye satellites are not strictly CubeSats but SmallSats (larger and heavier than CubeSats, (Sandau, 2010)), the processing needs for generating ARD of RapidEye images are essentially the same as for images from the CubeSats PlanetScope. Therefore, we used images from both constellations together to construct a longer time series than using PlanetScope images alone. Hereafter we shall refer to images from both constellations as CubeSat images for convenience. Limited by the total imagery volume available to this study, each acquired CubeSat image was restricted to a relatively small areal coverage of 5×5 km^2. In total, we collected RapidEye images on 38 dates from 2013 May to 2016 November and PlanetScope images on 80 dates from 2016 October to 2020 August. The acquisition time of these images ranged from 7:11 to 11:21 UTC. The solar zenith angle ranged from 30.2 to 79.0°. As to the Landsat-like images for the normalization, we used the SR images at 30-m resolution from the Harmonized Landsat Sentinel-2 (HLS, version 1.4) products that combine images from Landat-8 and Sentinel-2 satellites under common geometric gridding, spectral bandpass and view geometry (Claverie et al., 2018). As to the MODIS-like images for the evaluation of normalization, we used the daily SR images gridded at 500-m resolution from the MCD43A4 V006 product, the Nadir-BRDF (bidirectional reflectance distribution function) Adjusted Reflectance (NBAR), that is MODIS data corrected to a common nadir view geometry at the local solar noon zenith angle (Schaaf and Wang, 2015).

3.2. Processing Stage 1 & 2 in the HiNF

The Stage 1 & 2 match the radiometry of input target images (CubeSat images) to that of given reference images in similar processing steps but use different sources as reference images, which results in two levels of normalized CubeSat images. Both stages contain the same algorithms for radiometric normalization along with a quality control (QC) test. The QC test sorts normalized images in each stage into QC-compliant and QC-failed results. In the Stage 1, with Landsat-like SR images being the reference, the QC-compliant results are exported as level-1 normalized images. QC-failed results in the Stage 1 are largely caused by the failure of establishing a reliable radiometric transformation between CubeSat and Landsat-like images when clear corresponding pixels between two paired images are insufficient at the

coarser resolution of Landsat-like images. This insufficiency could be caused by contaminations of cloud/cloud shadow, limited areal coverages of available images, changes in landscapes, and a combination of these issues. All the normalized CubeSat images at level-1 from the Stage-1, with improved radiometric quality and much higher resolutions than Landsat-like images, serve as intermediate reference images in the Stage 2 to increase the chances of finding clear corresponding pixels between target and reference images for the normalization of the remaining CubeSat images with QC-failed results from the Stage 1. The QC-compliant results from the Stage 2 are exported as level-2 normalized images. The radiometric normalization procedure and the QC test in both stages are explained below.

3.2.1. Multi-date radiometric normalization

In both stages, per each target image on the date T_i we used reference images on multiple dates (R_j, $j = 1, 2 \ldots n$, and $n \leq 4$ in our demonstration) closest to T_i to generate a normalized CubeSat image on T_i. This multi-date radiometric normalization (Fig. 3) applies to both Stage 1 and 2. In the Stage 1, each target image out of all input CubeSat images was paired with multiple reference images on different dates from the HLS images. In the Stage 2, each of the remaining QC-failed CubeSat images from the Stage 1 was paired with multiple reference images from the level-1 normalized CubeSat images. The temporal difference between T_i and R_j was restricted under an upper limit (90 days in our demonstration) to avoid/reduce the impact of potential significant changes in land surface and differences in solar illumination angles. We chose the upper limit of 90 days for a good chance of cloud-free HLS images as reference images considering its longest repeat cycles in our study period (i.e., 16 days before 2015 by Landsat-8 alone) and reduced cloud-free revisits due to cloud coverages. The median number of days between the dates of one target and one reference images in our case was 20 days for the Stage 1 and 37 days for the Stage 2. Using the n reference images, we established multiple candidates of radiometric transformations using Iteratively Reweighted Multivariate Alteration Detection (IR-MAD) (Canty and Nielsen, 2008) to generate multiple candidates of normalized images per each target image. The IR-MAD detects invariant pixels between two images by applying canonical correlation analysis in iterations that place increasing focus on pixels whose change status is uncertain (Nielsen, 2007). We found invariant pixels between a target and a reference image by setting a threshold of 0.98 on the no-change probability given by the IR-MAD. The detected invariant pixels are then used in an orthogonal regression to establish the radiometric transformation from a target image to a reference.

Among multiple candidates of normalized images for each target image, we selected the best normalized image as the output for this target image using some predefined criteria. These criteria were the
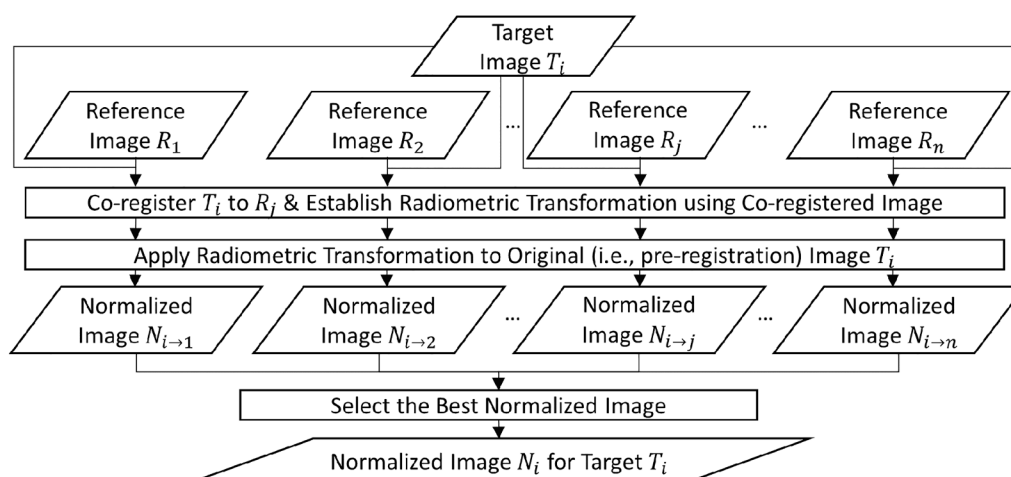

Fig. 3. Multi-date radiometric normalization approach that applies to both Stage 1 and Stage 2 in Fig. 2.

same as those in the quality control test and are described in the Section 3.2.2. To account for potential geometric misalignments between target and reference images, we co-registered a target image to each reference image using an algorithm called AROSICS (described in detail in the Section 3.3.2) before establishing radiometric transformations (Fig. 3). However, we generated normalized images by applying these transformations to the original (i.e., pre-registration) target image rather than a co-registered image. We chose this processing setup because the final geometric co-registration may be better achieved through images of greater radiometric consistency after Stage 1 & 2. In addition, resampling after radiometric normalization is needed to construct imagery time series in a common raster grid. To avoid resampling images twice, we did not resample images in Stage 1 & 2 for the co-registration purpose but used normalized images as inputs to the final co-registration in a two-step procedure in the Stage 3 as described later (Section 3.3.2).

The algorithm to establish radiometric transformations is the key in the Stage 1 & 2. The HiNF asks for an invariant-pixel-based algorithm (Du et al., 2002; Houborg and McCabe, 2018; Zhang et al., 2014) rather than the other commonly-used type of full-image-based algorithms such as the histogram matching (HM) (Wang et al., 2020). Invariant-pixel-based algorithms overcome possible changes (including contamination by cloud and cloud shadows) between target and reference images. Furthermore, it is relatively straightforward to design QC tests for such algorithms compared to full-image-based algorithms. Full-image-based algorithms usually require minimal changes between target and reference images (Hong and Zhang, 2008) and do not offer straightforward internal QC tests. In contrast, the QC tests for invariant-pixel-based algorithms can be readily achieved via the cross-validation technique by dividing detected invariant pixels into training and testing sets (Canty and Nielsen, 2008; Houborg and McCabe, 2018; Leach et al., 2019) as demonstrated in the next Section. While we chose the IR-MAD in our demonstration example because of its robustness against differing atmospheric conditions and its proven performances in our current and previous studies (Leach et al., 2019), future studies may test other existing and even develop new algorithms that detect invariant pixels in different ways and use one that best suits a user's region of interests and resources.

3.2.2. Quality control test in radiometric normalization

For the QC tests, we used two-thirds of detected invariant pixels to train an orthogonal regression and the remaining to test the normalization result. In case of different resolutions between target and reference images, target images were first resampled into the resolution of reference images using area-weighted average sampling. In the QC tests, post-normalization values of testing pixels in the target image were compared with pixel values of the reference image according to the following two statistical criteria, (1) the variance of testing pixel values in a CubeSat image after normalization was statistically comparable to that in the corresponding reference image for every band according to an F-test at a p-value of 0.1; (2) the linear correlation of testing pixel values between the post-normalization CubeSat image and the reference image was larger than 0.98 for every band. The normalization result for a pair of target and reference images was accepted if the comparison passed the above two criteria and otherwise was rejected. For each target image, we used the same two criteria to filter the multiple normalization candidates from using multiple reference images on different dates (Fig. 3). In case of more than one eligible candidate after passing through the two criteria, for each reference image candidate we calculated the ranges (maximum minus minimum) of reference surface reflectance values of training invariant pixels that were used in the regression at each of the four bands. We checked which candidate has the widest range at each band. We selected the normalized image for a given target image from using the reference candidate that has the greatest count of widest-range bands. A more reliable regression was expected by using invariant pixels that have wider ranges of reference values and hence a better radiometric transformation. We found this

criterion work well to select the best candidate after visually examining normalized candidate images and chose this criterion heuristically. In addition to the automatic QC test, one can optionally use visual inspection to further ensure the quality of normalized images from Stage 1 & 2. In our demonstration, the visual inspection removed one image from Stage-1 outputs and no image from Stage-2 outputs.

The two statistical criteria, the F-test of variances and the linear correlation of testing pixels before and after normalizations, can be used in the quality control test of normalized images by any invariant-pixel-based radiometric normalization algorithms.

3.3. Processing Stage 3 & 4 in the HiNF

The processing Stage 3 includes the following tasks,

(1) Flag non-target/poor-quality pixels by refining cloud masks (cloud and cloud shadows).
(2) Align CubeSat images into a common raster grid by geometric co-registration.
(3) Optionally generate daily mosaics for given regions of interests.

The optional generation of daily mosaics can be achieved by common algorithms implemented in many geospatial tools such as the GDAL programs (GDAL/OGR contributors, 2021) that is used in our demonstration example. The final processing Stage 4 is to evaluate the normalization efficacy using daily MODIS-like SR images. Because radiometric consistency through time is the focus of the evaluation, we choose MODIS-like SR images here that provide good benchmark of temporal variations thanks to its daily temporal resolution.

3.3.1. Refinement of cloud mask

While some optical CubeSat imagery products now come with cloud mask layers to help users mask out cloud and cloud shadows, these cloud masks may be insufficient for some downstream applications as was the case for this study. For example, Planet Labs Inc. provides a raster layer called Unusable Data Mask (UDM) and/or Usable Data Mask (UDM2) that can be used to flag cloud/cloud shadows in a CubeSat image (Planet Labs Inc., 2021a). However, UDM has been found unable to detect all cloud/cloud shadows as was the case for our demonstration example, necessitating extra processing by users to carry out appropriate time series analysis (Wang et al., 2020). The cloud/cloud shadows in UDM2 are detected by supervised machine learning techniques and the detection is believed to be better than UDM. However, UDM2 is only available back to the year 2018 and unavailable for a large amount of CubeSat images from the Planet Lab before 2018 (Planet Labs Inc., 2021b). Due to the complexity of cloud/cloud shadow detection, automatic detection of cloud/cloud shadows requires dedicated separate studies beyond the scope of this demonstration study. Here in addition to using the cloud mask from the UDM layer in the CubeSat images from the Planet Labs Inc., we manually masked out all the clouds and cloud shadows via visual inspection of the composites of CubeSat images in true color (red, green, blue bands as RGB channels) and false color (NIR, red, green bands as RGB channels) according to the characteristics of cloud/cloud shadows at the four bands given by Zhu and Woodcock (2012).

3.3.2. Two-step geometric co-registration

A two-step procedure of geometric co-registration is designed in the HiNF to align normalized CubeSat images into a common raster grid. In Step 1, cloud-free Landsat-like images are used as reference images to co-register same-day cloud-free CubeSat images. These Step-1 co-registered CubeSat images are then used in the Step 2 as the reference to co-register remaining CubeSat images. Each remaining CubeSat image is paired with a reference image that has the closest solar illumination angle and is acquired within ±90 days from the acquisition date of the image to be registered.

In our demonstration example, we identified 23 cloud-free pairs of

same-day CubeSat and HLS images for the geometric co-registration in Step 1. We chose an algorithm of geometric co-registration implemented as a Python-based package called AROSICS (Automated and Robust Open-Source Image Co-Registration Software; (Scheffler et al., 2017; Scheffler, 2021)) that provides out-of-the-box compatibility to multi-sensor and multi-temporal satellite data such as those used in our demonstration. The AROSICS directly handles unequal spatial and spectral characteristics between reference and target images and supports a wide range of projections and input data formats. Other approaches such as AROP (Gao et al., 2009), ARRSI (Wong and Clausi, 2007) or COSI-Corr (Leprince et al., 2007) have limitations in this regard, are more difficult to use or are not available as open-source software toolkits. Hence, they were less suited for our application. Additionally, AROSICS allows to customize output raster grids which enabled us to perform the resampling needed for correcting misregistrations and aligning output images into a common raster grid in a single step. This way, we could avoid resampling twice which would otherwise lead to an unnecessary degradation of geometric and radiometric quality. The underlying co-registration algorithm of AROSICS is based on phase correlation in the frequency domain, which makes it capable of sub-pixel alignment as well as robust against potential changes in images of different dates and also against interference of cloud/cloud shadows. This robustness was especially important in the context of our study area which covers a temporally dynamic wetland site with clear phenological and hydrological cycles. We used the local co-registration approach of AROSICS to compute around 25 tie-points per image pair. This allowed us to account for spatially varying misregistrations while keeping the computational load low. Computing more tie points was not needed in our case due to the rather flat terrain and the acquisition geometries of the sensors where we did not expect very complex distortions. For both the reference and target image, we used the near-infrared (NIR) band for tie-point generation because it provides the best spatial contrast in our study area. Tie points at cloud and cloud shadow positions were effectively filtered out by the three-step outlier detection algorithm implemented in AROSICS. We configured AROSICS to output co-registered images directly into a common raster grid of 5-m resolution.

To quantitatively assess the registration accuracy, we re-applied AROSICS to our co-registration results from the two steps of co-registration. We checked the residual errors and the overall RMSE value in the alignment between every pair of the CubeSat and HLS images before and after co-registration in the Step 1, as well as between every pair of the CubeSat images in the Step 2. Larger reduction in the residual errors indicates greater efficacy of geometric co-registration and hence better geometric co-registration accuracy.

3.3.3. Evaluation of normalization efficacy

Here we aim to quantitatively evaluate how effective the normalization is to match CubeSat images to Landsat-like images. However, CubeSat and Landsat-like images are not always acquired on the same days and do not have one-to-one temporal correspondence for direct comparison. Therefore, we used MODIS-like daily images as the bridging benchmark data for the evaluation of normalization efficacy. To do so, we resampled both CubeSat and Landsat-like images into the coarser raster grid of MODIS-like images using area-weighted resampling. If resultant coarser pixels were not fully covered by clear CubeSat or Landsat-like pixels, we excluded them in the subsequent analyses.

Given a band and a time period, we checked whether the similarity between CubeSat images and same-day MODIS-like benchmark images (here MCD43A4 products) gets closer to that between Landsat-like reference images (here HLS products) and same-day MODIS-like benchmark images after normalization compared to before normalization. We measured the MCD43A4-HLS and MCD43A4-CubeSat similarity in a time period at a band in two ways. In the first way, we used the slopes and intercepts from the linear regressions of MCD43A4 pixel values against coarsened HLS or CubeSat pixel values. If we see greater

reduction of differences in slopes and intercepts between MCD43A4-CubeSat and MCD43A4-HLS regressions after normalization, it means the CubeSat images are matched closer to the HLS images in terms of radiometric quality and the greater normalization efficacy. In the second way, we measured the similarity by root mean squared difference (*RMSD*). As in the first way, we checked the reduction of *RMSD* differences between MCD43A4-CubeSat and MCD43A4-HLS after normalization. We carried out the evaluation for the four spectral bands (B, G, R, NIR) as well as for the commonly-used normalized difference vegetation index ($NDVI = \frac{NIR-R}{NIR+R}$) (Tucker, 1979) by terrestrial ecosystem studies. For each band, we calculated the similarity measures for the entire study period of all the years and also for each year. Furthermore, to check whether the two levels of radiometric normalization from Stage 1 & 2 yielded similar efficacy, we tested whether the linear regression of the level-1 normalized CubeSat images against the same-day MCD43A4 is statistically similar to that of the level-2 normalized images. To test whether two linear regressions are statistically similar, we used Chow test (Chow, 1960) that is implemented in an R package 'gap' (Zhao, 2007).

Furthermore, we qualitatively evaluated the time series of CubeSat images before and after normalization. We randomly selected ten 30 × 30 m² regions of interests (ROIs, equal to one HLS pixel) over the study area and visually inspected the time series of average spectral band values and NDVI values within the ROIs from the pre-normalization CubeSat images, normalized CubeSat images, and reference HLS images. The calculation of an average is weighted by pixel fractions within a 30 × 30 m² ROI.

4. Results of the HiNF demonstration

4.1. Residual errors of geometric co-registration

By re-applying AROSICS to our co-registration results, we quantitatively evaluated the geometric co-registration accuracy of all the pairs of images in the co-registration. We found that the average residual errors in the alignment between CubeSat and HLS images were reduced from 9.99 m before the Step-1 co-registration to 4.80 m after the co-registration. This concurs with the findings of Scheffler et al. (2017) who obtained similar results in case of multi-sensor input images with large differences in spatial resolutions. The average residual errors in the alignment between two paired CubeSat images were reduced from 9.90 m before the Step-2 co-registration to 2.16 m after the co-registration. We also visually inspected randomly-selected pairs of CubeSat and HLS images in the Step-1 of geometric co-registration as well as pairs of CubeSat images in the Step-2 of geometric co-registration. The image pairs showed good and improved correspondence after the co-registration, which corroborates the improved geometric co-registration accuracy as indicated by the reduction in residual errors.

4.2. Time series of CubeSat images before and after normalization

Of the randomly-selected ten 30 × 30 m² ROIs to visualize time series of CubeSat images before and after normalization, we present the time series in two representative ROIs (Fig. 4 and Fig. 5) respectively over vegetation and water, two major surface cover types of interests at this wetland site. The other ROIs give us similar results regarding the similarity and differences in temporal variations of spectral band values and NDVI values. We see different temporal variations in the time series of pre-normalization CubeSat images and refence HLS images. The visible bands show larger differences in temporal variations between pre-normalization CubeSat images and reference HLS images than the NIR band. In contrast, the temporal variations in the time series of normalized CubeSat images and reference HLS images are better matched (see Section 4.3 for quantitative evaluation). In particular, we see two major improvements in the temporal consistency of imagery time series. First,
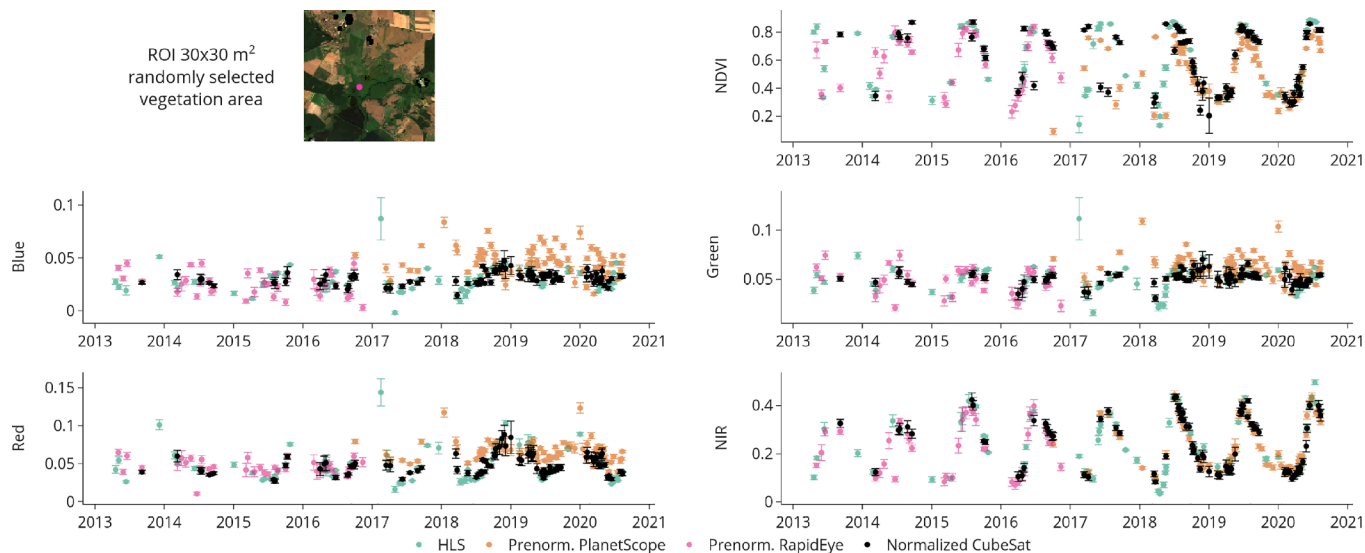
Fig. 4. Time series of the surface reflectance at the four spectral bands and the NDVI over a 30 × 30 m² region of interest (ROI). The ROI is randomly selected and is an area of vegetation. The dots in the time series are average pixel values weighted by pixel fractions within the ROI. The error bars are standard deviation of pixel values weighted by pixel fractions within the ROI. The background image in the upper left is the true-color composite of an HLS image of July 6th, 2018.

Fig. 5. Time series of the surface reflectance at the four spectral bands and the NDVI over a 30 × 30 m² region of interest (ROI). The ROI is randomly selected and is an area of water. The dots in the time series are average pixel values weighted by pixel fractions within the ROI. The error bars are standard deviation of pixel values weighted by pixel fractions within the ROI. The background image in the upper left is the true-color composite of an HLS image of July 6th, 2018.
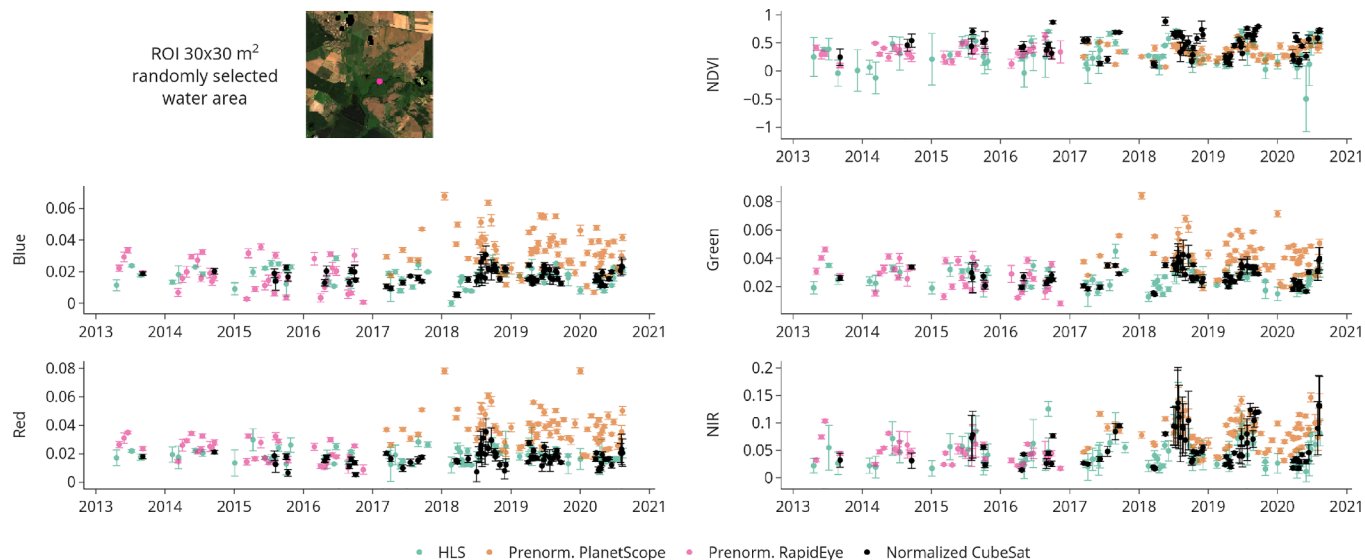
the temporal trajectories in pre-normalization PlanetScope images (orange dots in Fig. 4 and Fig. 5) show noticeable difference from those in reference HLS images, in particular at the blue band of the vegetation ROI and at all the visible bands of the water ROI. The normalized CubeSat images show comparable temporal trajectories at those bands with reference HLS images. Second, there is a clear discontinuity between prenormalization RapidEye and PlanetScope images, which is caused by differences in both the spectral responses of the sensors (see Fig. 3 in Wilson et al., 2017) and the radiometric qualities. After the normalization, the RapidEye and PlanetScope appear consistent with each other.

4.3. Quantitative evaluation of normalization efficacy

In Fig. 6, we plot the spectral band and NDVI values (each row) from the bridging benchmark images of MCD43A4 against those from the

CubeSat images (before and after normalization) as well as those from the reference HLS images over all the years. The scatter density plots between the MCD43A and the HLS images (the second column of Fig. 6) give the reference level of data distributions. The data distributions of MCD43A against pre-normalization CubeSat images (the first column of Fig. 6) deviate from those of MCD43A against HLS images. In particular, the visible bands show larger deviations than the NIR band, which agrees with what we see from the time series of spectral band values in the randomly selected ROIs. In contrast, the data distributions of MCD43A against normalized CubeSat images (the third to fifth columns of Fig. 6) appear similar to those of MCD43A against HLS images.

We further compared the slopes and intercepts of the linear regressions of the MCD43A4 respectively against the CubeSat (before and after normalization) and the HLS (Table 1). The linear regression coefficients of the HLS are the reference level. The normalized CubeSat images show coefficients much closer to the HLS than the pre-
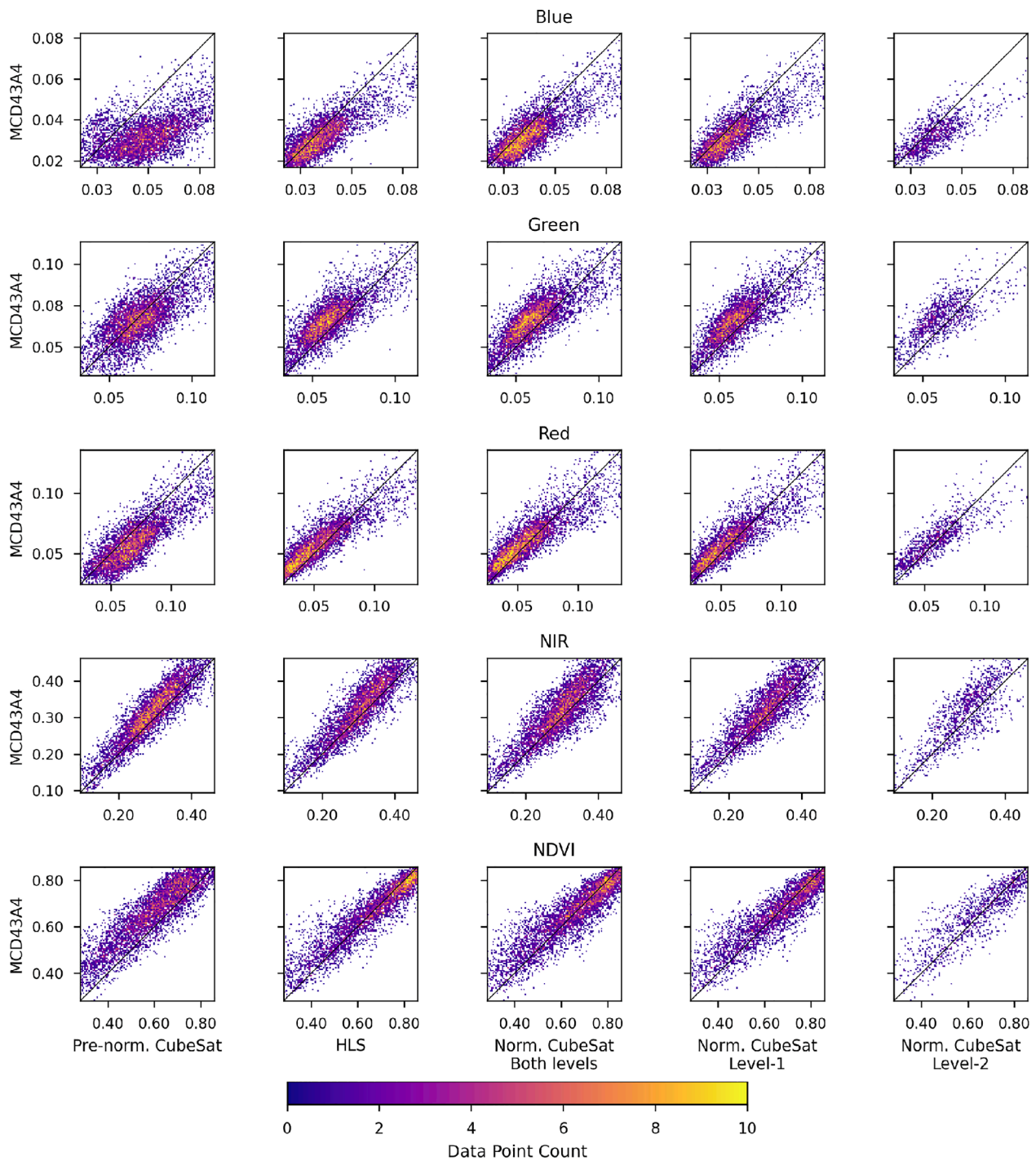
Fig. 6. Scatter density plots by comparing MCD43A images respectively (column-wise) against pre-normalization CubeSat images, HLS images, normalized CubeSat images of both processing levels, and normalized CubeSat images at normalization level-1 and level-2. Each row in the figure represents the four spectral bands and the NDVI.

Table 1
Equations of linear regressions with *y* being the benchmark MCD43A4 images and the *x* being respectively CubeSat (before and after normalization) and HLS images.

	Prenorm. CubeSat	HLS	Norm. CubeSatBoth levels	Norm. CubeSatLevel-1	Norm. CubeSatLevel-2
Image count	84	95	84	61	23
Blue	$y = 0.35x + 0.02$	$y = 0.60x + 0.01$	$y = 0.58x + 0.01$	$y = 0.60x + 0.01$	$y = 0.51x + 0.01$
Green	$y = 0.62x + 0.02$	$y = 0.68x + 0.02$	$y = 0.66x + 0.03$	$y = 0.68x + 0.02$	$y = 0.60x + 0.03$
Red	$y = 0.73x + 0.01$	$y = 0.69x + 0.02$	$y = 0.68x + 0.02$	$y = 0.69x + 0.02$	$y = 0.63x + 0.02$
NIR	$y = 0.97x + 0.03$	$y = 0.92x + 0.04$	$y = 0.86x + 0.06$	$y = 0.85x + 0.06$	$y = 0.87x + 0.06$
NDVI	$y = 0.80x + 0.18$	$y = 0.75x + 0.17$	$y = 0.72x + 0.19$	$y = 0.72x + 0.19$	$y = 0.73x + 0.18$

normalization CubeSat images do for all the spectral bands except the NIR band, indicating good normalization efficacy for the visible bands but less efficacy for the NIR band. The linear regressions of the level-1 normalized CubeSat images against the MCD43A4 were statistically similar to those of the level-2 against the MCD43A4 for the NIR band and the NDVI but not so for the visible bands according to the Chow test (at significance level of 0.05). This result indicated similar normalization efficacy of the two normalization levels for the NIR band and the NDVI but less similar for the visible bands.

The Table 2 lists the MCD43A4-HLS *RMSD* along with the MCD43A4-CubeSat *RMSD* before and after normalization using images of all the years. The relative differences between MCD43A4-CubeSat *RMSD* and MCD43A4-HLS *RMSD* (absolute differences divided by MCD43A4-HLS *RMSD*) are also given in Fig. 7 using images from all the years and also from each year before and after normalization. The MCD43A4-HLS *RMSD* is the reference level of image similarity that the HiNF is expected to achieve. The smaller the difference between MCD43A4-HLS *RMSD* and MCD43A4-CubeSat *RMSD*, the closer CubeSat images are to the reference HLS images in terms of radiometric quality. A larger reduction in the *RMSD* difference indicates better normalization efficacy. For images of all the years, the normalized CubeSat images at the level-1 give *RMSD* closer to the HLS images than the pre-normalization CubeSat images do for all the bands and the NDVI. At the level-2, we see similar pattern except for the NIR band, indicating lower radiometric quality of normalized level-2 images. For images per each year, we generally see similar patterns of the reduction in *RMSD* differences in normalized CubeSat images at the two levels. Overall, the quantitative evaluation suggests stronger normalization efficacy at visible bands than the NIR band and the NDVI.

5. Discussion

The areal coverage of CubeSat images available to this study was relatively small (5×5 km^2) but covered a spatially heterogeneous and temporally dynamic wetland site. This study scenario motivated us to set up a framework called HiNF to generate long and consistent times series of 5-m CubeSat images and to quantitatively evaluate its normalization efficacy. The relatively small imagery area was more demanding on the spatial resolution of reference images than otherwise for image normalization to obtain sufficient corresponding pixels between paired CubeSat and reference images. To address this challenge in the HiNF, we used Landsat-like images (HLS dataset) as the reference images in the Stage-1 processing and additionally used normalized CubeSat images from the Stage-1 (i.e., level-1 normalized images) as reference images in the Stage-2 processing. The use of level-1 normalized CubeSat images in a second-stage normalization allowed the QC-compliant normalization results to increase from 61 images to 84 images out of total input 118 images to be normalized. After visually checking the 34 CubeSat images that failed to produce QC-compliant normalization results, we found majority of them in particular poor quality that were better to be excluded from our imagery time series. The Chow test suggests similar normalization efficacies of the two normalization stages for the NIR band and the NDVI but less so for the visible bands. After the

normalization at both levels, we generally see reduction in the differences between MCD43A4-CubeSat *RMSD* and MCD43A4-HLS *RMSD* in most years though the level-1 usually shows greater reduction. However, the *RMSD* differences in some years (e.g., 2016) remain larger after the level-2 normalization rather than reduced, which indicates particularly low quality of the level-2 normalized images in these years. The explicit labelling of level-1 and level-2 allows downstream applications to balance the tradeoff between the quality and the quantity of available normalized CubeSat images in a time series.

While the hectometer resolutions of MODIS-like images make them much less desirable as reference images to normalized CubeSat images, their daily availability allows us to use them in the quantitative evaluation of normalization efficacy as bridging benchmark images to pair with same-day CubeSat images as well as with same-day reference Landsat-like images. By pooling paired same-day imagery pixels over a period and a region at the resolution of MODIS-like images (here MCD43A4), we were able to measure the MCD43A4-HLS similarity in the form of linear regression coefficients and *RMSD* as the reference level of similarity that the MCD43A4-CubeSat similarity could be quantitatively compared against. Such similarity measures allow us to quantitatively evaluate normalization efficacies for different bands, different periods, and different regions. In our demonstration, we carried out the evaluation by pooling pixels over relatively long periods (each year and all the years) in the entire available imagery region (5×5 km^2). If the resources of a study permit larger coverages and denser time series of CubeSat images, finer-grained evaluations of normalization efficacy can be carried out at shorter periods (such as monthly, weekly or even daily) and smaller areal subsets (such per 1×1 km^2 or even per MODIS pixel). With larger-area CubeSat images, we can further afford constraining evaluation areas to MODIS pixels that are spatially-homogenous according to same-day CubeSat and Landsat-like images. This additional constraint avoids spectrally-mixed pixels at the MODIS-like resolutions and likely improves the quantitative evaluation because the best normalization based on highly-mixed pixels at the MODIS resolution may not necessarily indicate the best at the CubeSat resolutions. Furthermore, due to relatively small areal coverage of CubeSat images in our study, we did not have enough MODIS pixels to carry out robust co-registration between CubeSat and MODIS images before calculating their similarity. In case of sufficiently large areal coverages of CubeSat images, geometric co-registration between CubeSat (as well as Landsat-like) and MODIS images will improve the calculation of similarity measures and refine the results of the quantitative evaluation. We also note that the spatial effective resolution of MCD43A4 products may be larger than its nominal grid size of 500 m because this product combines observations from many different view angles that lead to varying ground sampling distances given the point spread function (PSF) of the MODIS sensors (Campagnolo et al., 2016; Campagnolo and Montaño, 2014). A further refinement of the evaluation should consider the spatial effective resolution of the MCD43A4 products and convolve with the MODIS PSF when aggregating CubeSat/Landsat-like pixels.

The quantitative evaluation using MODIS-like images as bridging benchmark data reveals that in our demonstration the normalization efficacies for the visible bands were higher than for the NIR band, which agreed with what we saw from the visual inspection of time series of spectral band and NDVI values in 30×30 m^2 ROIs. The temporal consistency of the NDVI time series was thus restricted by the normalization quality of the NIR band. The current normalization probably overcorrected the NIR band. Land surface, especially with vegetation covers, has larger variations in reflectance values at the NIR band than the visible bands (e.g., Fig. 4), which may require more paired invariant pixels between CubeSat and reference images to establish reliable radiometric transformations. The relatively small areal coverage of available CubeSat images may have provided enough paired invariant pixels for the visible bands but not enough for the NIR band to cover its wider ranges of variations, which can partially explain the lower normalizing efficacy for the NIR band. Additionally, much of this
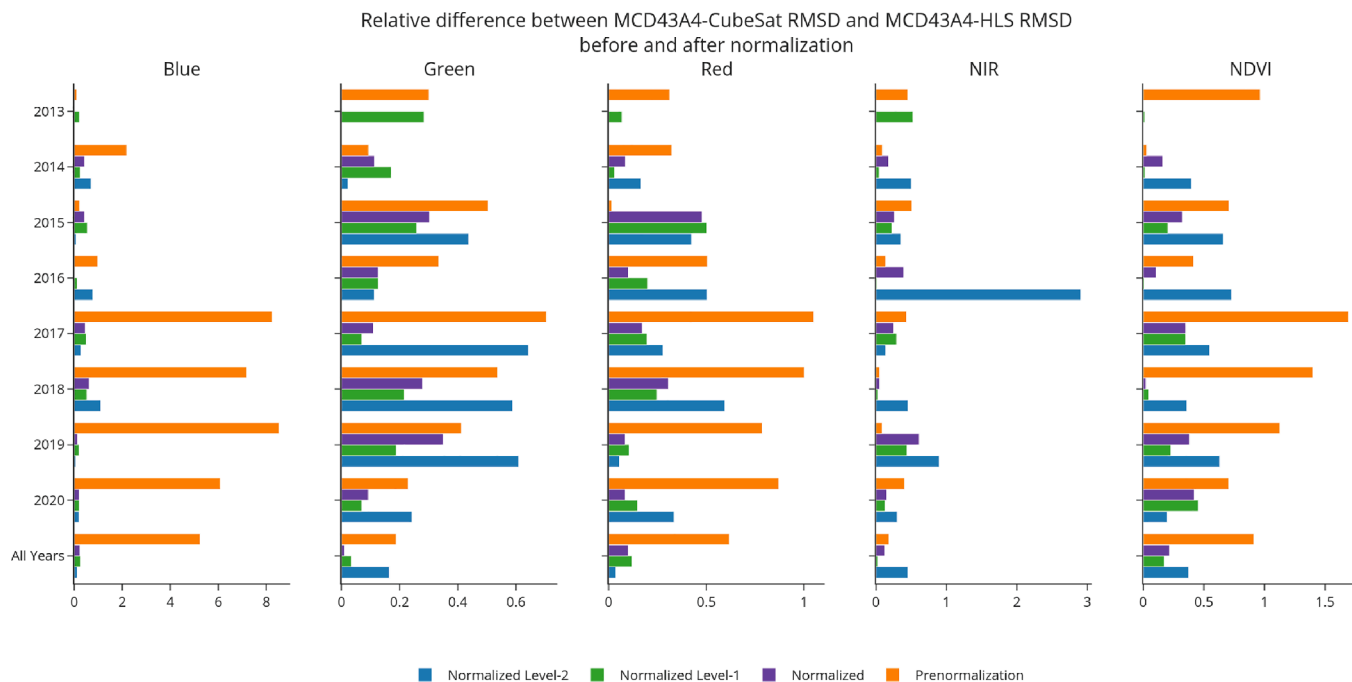
Table 2
The *RMSD* from comparing the benchmark MCD43A4 images respectively against the CubeSat images (before and after normalization) and the HLS images.

	Prenorm. CubeSat	HLS	Norm. CubeSat Both levels	Norm. CubeSat Level-1	Norm. CubeSat Level-2
Blue	0.022	0.009	0.010	0.010	0.009
Green	0.012	0.011	0.011	0.011	0.012
Red	0.016	0.013	0.013	0.013	0.013
NIR	0.039	0.043	0.045	0.043	0.051
NDVI	0.091	0.066	0.073	0.071	0.077

Fig. 7. Relative differences between MCD43A4-CubeSat RMSD and MCD43A4-HLS RMSD before and after the normalization of CubeSat images. Smaller differences (shorter bar) are better, indicating radiometric quality of CubeSat closer to the reference HLS. Note that the normalized CubeSat images in 2013 are all at level-1.

wetland site was flooded over several months every year. Water surfaces show more pronounced improvements of radiometric quality after normalization at visible bands than the NIR as indicated by Fig. 5. Collectively, we see greater normalization efficacy at the visible bands than the NIR in our study area. This finding is different from Leach et al. (2019) that suggests better normalization efficacy at longer wavelengths in a much larger and forest-dominated area. In that study, the haze from forest fires was the major issue that caused greater trouble in the normalization of shorter-wavelength bands. In contrast, there was no haze in the CubeSat images in our study, but rather the water-saturated area was the challenging issue for the normalization. Furthermore, a single radiometric transformation for entire images may not be sufficient for the NIR band because larger variations at the NIR band imply the relationship between pixels of CubeSat and reference images may vary more across different land surface types/conditions. More sophisticated algorithms of radiometric normalization are needed to improve the normalization efficacy at the NIR band. For example, an algorithm that uses radiometric transformations specific to land covers could be explored as recently done for the harmonization of Landsat-8 and Sentinel-2 data (Scheffler et al., 2020).

The detection of cloud and cloud shadow is crucial for moving towards operational CubeSat ARD and another critical procedure of the HiNF that requires further studies. Two possible options may be promising for an automatic detection. The first is to examine whether machine-learning-based approaches can be expanded to different optical CubeSat images based on the generation of the UDM2 that is only available for post-2018 PlanetScope images (Planet Labs Inc., 2021b). Alternatively, further studies can examine whether time series information can be used to filter cloud/cloud shadow either before normalization or after normalization in a way similar to the Tmask approach that has improved cloud/cloud shadow detection in Landsat images (Zhu and Woodcock, 2014).

The radiometric quality of optical CubeSat images will likely improve as commercial off-the-shelf optical sensors keep getting better and preprocessing methods by data providers prior to data distribution also improve. However, the reliance on large well-calibrated sun-synchronous optical satellite missions to normalize optical CubeSat images is likely to stay in the foreseeable future. The normalization using

images from large well-calibrated satellites is not only to address differences in sensor performance but also to normalize sun-sensor geometry in many images acquired by so many CubeSats. Large numbers of satellites in CubeSat constellations imply quite different satellite overpass times and hence quite different solar angles that need to be normalized into a common/similar sun-sensor geometry to produce ARD of optical CubeSat images. A few large well-calibrated sun-synchronous satellites (e.g., MODIS, Landsat, Sentinel-2) have similar overpass times and can be readily corrected to provide BRDF-normalized images (Roy et al., 2016, 2017) as the input data for the correction of sun-sensor geometry of CubeSat images. Furthermore, different solar illumination angles also cause varying target shadows and hence different texture in acquired images. Such shadow-induced differences in image texture are particularly noticeable in VHR CubeSat images, which causes anomalies in the frequency domain of images. Since AROSICS is based on the phase correlation in the frequency domain, a large difference in solar illumination angles between reference and target images may decrease the co-registration accuracy. For better co-registration results, we chose to pair images in a way that respects the solar illumination angle (Section 3.3.2). However, further research is needed to improve the co-registration performance for VHR images acquired with large differences in sun-sensor geometries.

6. Conclusion

The HiNF was demonstrated at a spatially heterogeneous and temporally dynamic wetland site to generate temporally consistent stack of VHR optical CubeSat images at a ~ biweekly interval over 8 years. Given the relatively small areal coverages of images available to the demonstration study, a novel two-stage procedure in the HiNF successfully normalized more CubeSat images than using Landsat-like reference images (HLS products) in one stage alone did. The two-stage procedure explicitly flags normalized images with level-1 and level-2 as a quality indicator. The two levels of normalized images allow downstream applications to balance the tradeoff between the quality and the quantity of available normalized CubeSat images in a time series. A new quantitative approach to evaluating normalization efficacy was developed by using MODIS-like daily images at hectometer

resolutions (MCD43A4 products) as the bridging benchmark data to pair same-day MCD43A4 images with both HLS and CubeSat images. By comparing quantitative measures of MCD43A4-HLS similarity against MCD43A4-CubeSat similarity before and after normalization, we were able to quantify the normalization efficacy at the two normalization levels for the four spectral bands and the NDVI. The evaluation results indicated similar normalization efficacy of the two normalization levels for the NIR band and the NDVI but less so for the visible bands. The visible bands showed greater normalization efficacy than the NIR band and the NDVI, which warrants further development of more sophisticated algorithms to improve the normalization of the NIR band for such wetland areas as our study site. As more applications try to take advantage of burgeoning optical CubeSat images, the HiNF, an effective and flexible framework for normalizing optical CubeSat images along with the presented quantitative evaluation approach, facilitates the generation and the quality assurance of analysis ready data of optical CubeSat images.

CRediT authorship contribution statement

Zhan Li: Conceptualization, Methodology, Software, Validation, Formal analysis, Resources, Writing – original draft, Writing – review & editing, Visualization. **Daniel Scheffler:** Software, Validation, Formal analysis, Writing – original draft, Writing – review & editing. **Nicholas C. Coops:** Resources, Writing – review & editing. **Nicholas Leach:** Software, Writing – review & editing. **Torsten Sachs:** Writing – original draft, Writing – review & editing, Funding acquisition.

Declaration of Competing Interest

The authors declare that they have no known competing financial interests or personal relationships that could have appeared to influence the work reported in this paper.

Acknowledgements

References

Aragon, B., Houborg, R., Tu, K., Fisher, J.B., McCabe, M., 2018. CubeSats enable high spatiotemporal retrievals of crop-water use for precision agriculture. Remote Sensing 10, 1867. https://doi.org/10.3390/rs10121867.

Cai, Y., Guan, K., Nafziger, E., Chowdhary, G., Peng, B., Jin, Z., Wang, S., Wang, S., 2019. Detecting In-season crop nitrogen stress of corn for field trials using UAV- and CubeSat-based multispectral sensing. IEEE J. Sel. Top. Appl. Earth Obs. Remote Sens. 12, 5153–5166. https://doi.org/10.1109/JSTARS.2019.2953489.

Campagnolo, M.L., Montaño, E.L., 2014. Estimation of effective resolution for Daily MODIS gridded surface reflectance products. IEEE Trans. Geosci. Remote Sens. 52, 5622–5632. https://doi.org/10.1109/TGRS.2013.2291496.

Campagnolo, M.L., Sun, Q., Liu, Y., Schaaf, C., Wang, Z., Román, M.O., 2016. Estimating the effective spatial resolution of the operational BRDF, albedo, and nadir reflectance products from MODIS and VIIRS. Remote Sens. Environ. 175, 52–64. https://doi.org/10.1016/j.rse.2015.12.033.

Canty, M.J., Nielsen, A.A., Schmidt, M., 2004. Automatic radiometric normalization of multitemporal satellite imagery. Remote Sens. Environ. 91, 441–451. https://doi.org/10.1016/j.rse.2003.10.024.

Canty, M.J., Nielsen, A.A., 2008. Automatic radiometric normalization of multitemporal satellite imagery with the iteratively re-weighted MAD transformation. Remote Sens. Environ. 112, 1025–1036. https://doi.org/10.1016/j.rse.2007.07.013.

CEOS, 2021. CEOS Analysis Ready Data [WWW Document]. URL https://ceos.org/ard/index.html#slide2 (accessed 2.22.21).

Chander, G., Xiong, X. (J), Choi, T. (J), Angal, A., 2010. Monitoring on-orbit calibration stability of the Terra MODIS and Landsat 7 ETM+ sensors using pseudo-invariant test sites. Remote Sensing Environ. 114, 925–939. doi: 10.1016/j.rse.2009.12.003.

Chow, G.C., 1960. Tests of equality between sets of coefficients in two linear regressions. Econometrica 28, 591–605. https://doi.org/10.2307/1910133.

Claverie, M., Ju, J., Masek, J.G., Dungan, J.L., Vermote, E.F., Roger, J.-C., Skakun, S.V., Justice, C., 2018. The harmonized landsat and sentinel-2 surface reflectance data set. Remote Sens. Environ. 219, 145–161. https://doi.org/10.1016/j.rse.2018.09.002.

Cooley, S.W., Smith, L.C., Ryan, J.C., Pitcher, L.H., Pavelsky, T.M., 2019. Arctic-Boreal lake dynamics revealed using CubeSat imagery. Geophys. Res. Lett. 46, 2111–2120. https://doi.org/10.1029/2018GL081584.

Dash, J., Ogutu, B.O., 2016. Recent advances in space-borne optical remote sensing systems for monitoring global terrestrial ecosystems. Progress Phys. Geography: Earth Environ. 40, 322–351. https://doi.org/10.1177/0309133316639403.

Du, Y., Teillet, P.M., Cihlar, J., 2002. Radiometric normalization of multitemporal high-resolution satellite images with quality control for land cover change detection. Remote Sens. Environ. 82, 123–134. https://doi.org/10.1016/S0034-4257(02)00029-9.

Dwyer, J.L., Roy, D.P., Sauer, B., Jenkerson, C.B., Zhang, H.K., Lymburner, L., 2018. Analysis ready data: Enabling analysis of the landsat archive. Remote Sensing 10, 1–19. https://doi.org/10.3390/rs10091363.

FLUXNET Network, 2021. About the FLUXNET Network [WWW Document]. FLUXNET. URL https://fluxnet.org/about/ (accessed 5.4.21).

Frantz, D., 2019. FORCE—Landsat + Sentinel-2 Analysis Ready Data and Beyond. Remote Sensing 11, 1124. https://doi.org/10.3390/rs11091124.

Franz, D., Koebsch, F., Larmanou, E., Augustin, J., Sachs, T., 2016. High net CO 2 and CH 4 release at a eutrophic shallow lake on a formerly drained fen. Biogeosciences 13, 3051–3070. https://doi.org/10.5194/bg-13-3051-2016.

Gao, F., Masek, J.G., Wolfe, R.E., 2009. Automated registration and orthorectification package for Landsat and Landsat-like data processing 3, 33515–33520.

GDAL/OGR contributors, 2021. GDAL/OGR Geospatial Data Abstraction software Library.

Hong, G., Zhang, Y., 2008. A comparative study on radiometric normalization using high resolution satellite images. Int. J. Remote Sens. 29, 425–438. https://doi.org/10.1080/01431160601086019.

Houborg, R., McCabe, M.F., 2018. A Cubesat enabled Spatio-Temporal Enhancement Method (CESTEM) utilizing Planet, Landsat and MODIS data. Remote Sens. Environ. 209, 211–226. https://doi.org/10.1016/j.rse.2018.02.067.

Houborg, R., McCabe, M.F., 2016. High-Resolution NDVI from Planet's Constellation of Earth Observing Nano-Satellites: A New Data Source for Precision Agriculture. Remote Sensing 8, 768. https://doi.org/10.3390/rs8090768.

Kimm, H., Guan, K., Jiang, C., Peng, B., Gentry, L.F., Wilkin, S.C., Wang, S., Cai, Y., Bernacchi, C.J., Peng, J., Luo, Y., 2020. Deriving high-spatiotemporal-resolution leaf area index for agroecosystems in the U.S. Corn Belt using Planet Labs CubeSat and STAIR fusion data. Remote Sens. Environ. 239, 111615. https://doi.org/10.1016/j.rse.2019.111615.

Koebsch, F., Gottschalk, P., Beyer, F., Wille, C., Jurasinski, G., Sachs, T., 2020. The impact of occasional drought periods on vegetation spread and greenhouse gas exchange in rewetted fens. Philosoph. Trans. Roy. Soc. B: Biol. Sci. 375, 20190685. https://doi.org/10.1098/rstb.2019.0685.

Leach, N., Coops, N.C., Obrknezev, N., 2019. Normalization method for multi-sensor high spatial and temporal resolution satellite imagery with radiometric inconsistencies. Comput. Electron. Agric. 164, 104893. https://doi.org/10.1016/j.compag.2019.104893.

Lee, S., Hutputanasin, A., Toorian, A., Lan, W., Munakata, R., Carnahan, J., Pignatelli, D., Mehrparvar, A., Johnstone, A., 2020. CubeSat Design Specification Rev. 14 The CubeSat Program, Cal Poly SLO (No. CP-CDS-R14). Cal Poly, San Luis Obispo, CA.

Leprince, S., Barbot, S., Ayoub, F., Avouac, J.-P., 2007. Automatic and Precise Orthorectification, Coregistration, and Subpixel Correlation of Satellite Images, Application to Ground Deformation Measurements. IEEE Trans. Geosci. Remote Sens. 45, 1529–1558. https://doi.org/10.1109/TGRS.2006.888937.

McCabe, M.F., Rodell, M., Alsdorf, D.E., Miralles, D.G., Uijlenhoet, R., Wagner, W., Lucieer, A., Houborg, R., Verhoest, N.E.C., Franz, T.E., Shi, J., Gao, H., Wood, E.F., 2017. The Future of Earth Observation in Hydrology. Hydrol. Earth Syst. Sci. 21, 3879–3914. https://doi.org/10.5194/hess-21-3879-2017.

Nielsen, A.A., 2007. The Regularized Iteratively Reweighted MAD Method for Change Detection in Multi- and Hyperspectral Data. IEEE Trans. Image Process. 16, 463–478. https://doi.org/10.1109/TIP.2006.888195.

Planet Labs Inc., 2021a. Planet imagery product specifications. Planet Labs Inc., San Francisco, CA, USA.

Planet Labs Inc., 2021b. UDM 2 [WWW Document]. URL https://developers.planet.com/docs/data/udm-2/ (accessed 3.22.21).

Poghosyan, A., Golkar, A., 2017. CubeSat evolution: Analyzing CubeSat capabilities for conducting science missions. Prog. Aerosp. Sci. 88, 59–83. https://doi.org/10.1016/j.paerosci.2016.11.002.

Puig-Suari, J., Turner, C., Twiggs, R., 2001. CubeSat: the development and launch support infrastructure for eighteen different satellite customers on one launch. In: Proceedings of the Small Satellite Conference. Utah State University, Logan, Utah, USA, pp. SSC01-VIIIb-5.

Riihimäki, H., Luoto, M., Heiskanen, J., 2019. Estimating fractional cover of tundra vegetation at multiple scales using unmanned aerial systems and optical satellite data. Remote Sens. Environ. 224, 119–132. https://doi.org/10.1016/j.rse.2019.01.030.

Roy, D.P., Li, J., Zhang, H., Yan, L., Huang, H., Li, Z., 2017. Examination of Sentinel-2A multi-spectral instrument (MSI) reflectance anisotropy and the suitability of a general method to normalize MSI reflectance to nadir BRDF adjusted reflectance. Remote Sens. Environ. 199, 25–38. https://doi.org/10.1016/j.rse.2017.06.019.

Roy, D.P., Zhang, H., Ju, J., Gomez-Dans, J.L., Lewis, P.E., Schaaf, C., Sun, Q., Li, J., Huang, H., Kovalskyy, V., 2016. A general method to normalize Landsat reflectance data to nadir BRDF adjusted reflectance. Remote Sens. Environ. 176, 255–271. https://doi.org/10.1016/j.rse.2016.01.023.

Sandau, R., 2010. Status and trends of small satellite missions for Earth observation. Acta Astronaut. 66, 1–12. https://doi.org/10.1016/j.actaastro.2009.06.008.

Santilli, G., Vendittozzi, C., Cappelletti, C., Battistini, S., Gessini, P., 2018. CubeSat constellations for disaster management in remote areas. Acta Astronaut. 145, 11–17. https://doi.org/10.1016/j.actaastro.2017.12.050.

Schaaf, C., Wang, Z., 2015. MCD43A4 MODIS/Terra+Aqua BRDF/Albedo Nadir BRDF Adjusted Ref Daily L3 Global - 500m V006. doi: 10.5067/MODIS/MCD43A4.006.

Scheffler, D., Hollstein, A., Diedrich, H., Segl, K., Hostert, P., 2017. AROSICS: An Automated and Robust Open-Source Image Co-Registration Software for Multi-Sensor Satellite Data. Remote Sensing 9, 676. https://doi.org/10.3390/rs9070676.

Scheffler, D., Frantz, D., Segl, K., 2020. Spectral harmonization and red edge prediction of Landsat-8 to Sentinel-2 using land cover optimized multivariate regressors. Remote Sens. Environ. 241, 111723. https://doi.org/10.1016/j.rse.2020.111723.

Scheffler, D., 2021. AROSICS: An Automated and Robust Open-Source Image Co-Registration Software for Multi-Sensor Satellite Data. Zenodo. https://doi.org/10.5281/zenodo.4601166.

Selva, D., Krejci, D., 2012. A survey and assessment of the capabilities of Cubesats for Earth observation. Acta Astronaut. 74, 50–68. https://doi.org/10.1016/j.actaastro.2011.12.014.

Tucker, C.J., 1979. Red and Photographic Infrared Linear Combinations for Monitoring Vegetation. Remote Sens. Environ. 8, 127–150.

Wang, J., Yang, D., Detto, M., Nelson, B.W., Chen, M., Guan, K., Wu, S., Yan, Z., Wu, J., 2020. Multi-scale integration of satellite remote sensing improves characterization of dry-season green-up in an Amazon tropical evergreen forest. Remote Sens. Environ. 246, 111865. https://doi.org/10.1016/j.rse.2020.111865.

Wegmueller, S.A., Leach, N.R., Townsend, P.A., 2021. LOESS radiometric correction for contiguous scenes (LORACCS): Improving the consistency of radiometry in high-resolution satellite image mosaics. Int. J. Appl. Earth Obs. Geoinf. 97, 102290. https://doi.org/10.1016/j.jag.2020.102290.

Wilson, N., Greenberg, J., Jumpasut, Arin, Collison, Alan, Weichelt, Horst, 2017. Absolute Radiometric Calibration of Planet Dove Satellites, Flocks 2p & 2e. Planet Labs Inc., San Francisco, CA, USA.

Wong, A., Clausi, D.A., 2007. ARRSI: Automatic Registration of Remote-Sensing Images. IEEE Trans. Geosci. Remote Sens. 45, 1483–1493. https://doi.org/10.1109/TGRS.2007.892601.

Wu, S., Wang, J., Yan, Z., Song, G., Chen, Y., Ma, Q., Deng, M., Wu, Y., Zhao, Y., Guo, Z., Yuan, Z., Dai, G., Xu, X., Yang, X., Su, Y., Liu, L., Wu, J., 2021. Monitoring tree-crown scale autumn leaf phenology in a temperate forest with an integration of PlanetScope and drone remote sensing observations. ISPRS J. Photogramm. Remote Sens. 171, 36–48. https://doi.org/10.1016/j.isprsjprs.2020.10.017.

Wulder, M.A., Loveland, T.R., Roy, D.P., Crawford, C.J., Masek, J.G., Woodcock, C.E., Allen, R.G., Anderson, M.C., Belward, A.S., Cohen, W.B., Dwyer, J., Erb, A., Gao, F., Griffiths, P., Helder, D., Hermosilla, T., Hipple, J.D., Hostert, P., Hughes, M.J., Huntington, J., Johnson, D.M., Kennedy, R., Kilic, A., Li, Z., Lymburner, L., McCorkel, J., Pahlevan, N., Scambos, T.A., Schaaf, C., Schott, J.R., Sheng, Y., Storey, J., Vermote, E., Vogelmann, J., White, J.C., Wynne, R.H., Zhu, Z., 2019. Current status of Landsat program, science, and applications. Remote Sens. Environ. 225, 127–147. https://doi.org/10.1016/j.rse.2019.02.015.

Zhang, L., Wu, C., Du, B., 2014. Automatic Radiometric Normalization for Multitemporal Remote Sensing Imagery With Iterative Slow Feature Analysis. IEEE Trans. Geosci. Remote Sens. 52, 6141–6155. https://doi.org/10.1109/TGRS.2013.2295263.

Zhao, J.H., 2007. gap: Genetic Analysis Package. J. Stat. Softw. 23, 1–18. https://doi.org/10.18637/jss.v023.i08.

Zhu, Z., Woodcock, C.E., 2012. Object-based cloud and cloud shadow detection in Landsat imagery. Remote Sens. Environ. 118, 83–94. https://doi.org/10.1016/j.rse.2011.10.028.

Zhu, Z., Woodcock, C.E., 2014. Automated cloud, cloud shadow, and snow detection in multitemporal Landsat data: An algorithm designed specifically for monitoring land cover change. Remote Sens. Environ. 152, 217–234. https://doi.org/10.1016/j.rse.2014.06.012.